

Two-dimensional magnetic nanoelectromechanical resonators

Shengwei Jiang¹, Hongchao Xie¹, Jie Shan^{1,2,3*}, Kin Fai Mak^{1,2,3*}

¹Laboratory of Atomic and Solid State Physics, Cornell University, Ithaca, NY, USA.

²School of Applied and Engineering Physics, Cornell University, Ithaca, NY, USA

³Kavli Institute at Cornell for Nanoscale Science, Ithaca, NY, USA

Email: jie.shan@cornell.edu; kinfai.mak@cornell.edu

These authors contributed equally: Shengwei Jiang, Hongchao Xie.

Two-dimensional (2D) layered materials possess outstanding mechanical, electronic and optical properties, making them ideal materials for nanoelectromechanical applications^{1,2}. The recent discovery of 2D magnetic materials^{3,4,5,6,7,8} has promised a new class of magnetically active nanoelectromechanical systems (NEMS). Here we demonstrate resonators made of 2D CrI₃, whose mechanical resonances depend on the magnetic state of the material. We quantify the underlining effects of exchange and anisotropy magnetostriction by measuring the field dependence of the resonance frequency under a magnetic field parallel and perpendicular to the easy axis, respectively. Furthermore, we show efficient strain tuning of magnetism in 2D CrI₃ as a result of the inverse magnetostrictive effect using the NEMS platform. Our results establish the basis for mechanical detection of magnetism and magnetic phase transitions in 2D layered magnetic materials. The new magnetic NEMS may also find applications in magnetic actuation and sensing.

Two-dimensional (2D) layered magnetic materials are attractive building blocks for nanoelectromechanical systems (NEMS): while they share high stiffness and strength and low mass with other 2D materials, they are magnetically active^{1,2,3,6,7,8}. Among the large class of newly emerged 2D layered magnetic materials, of particular interest is few-layer CrI₃, whose magnetic ground state consists of antiferromagnetically coupled ferromagnetic (FM) monolayers with out-of-plane easy axis^{3,5}. The interlayer exchange interaction is relatively weak, a magnetic field on the order of 0.5 T in the out-of-plane (\hat{z}) direction can induce spin-flip transition in bilayer CrI₃. Remarkable phenomena and device concepts based on detecting and controlling the interlayer magnetic state have been recently demonstrated, including spin-filter giant magnetoresistance^{9,10,11,12}, magnetic switching by electric field¹³ or electrostatic doping^{14,15,16,17}, and spin transistors¹⁸. The coupling between the magnetic and mechanical properties in atomically thin materials, the basis for 2D magnetic NEMS, however, remains elusive although NEMS made of thicker magnetic materials¹⁹ or coated with FM metals^{20,21} have been studied.

Here we demonstrate magnetic NEMS resonators made of 2D CrI₃ drumhead membranes and investigate magnetostriction and its inverse effect in the material (Fig. 1a). We focus

on even-layer CrI₃ for maximum effect. We encapsulate CrI₃ (an air sensitive insulator) within two stable 2D materials, few-layer graphene (below) and monolayer WSe₂ (above) (Fig. 1b). In addition to protect CrI₃ from degradation under ambient conditions, few-layer graphene acts as a conducting electrode, while monolayer WSe₂ as a strain gauge as we discuss below. The 2D heterostructure was first assembled and then transferred on prefabricated circular microtrenches (2 – 3 μm in radius) with patterned Au electrodes and Si back gate. The optical image of a sample device is shown in Fig. 1c. We drive mechanical resonances in the membrane electrically in the linear regime using a small r.f. gate voltage, which is superposed on a DC gate voltage V_g that applies static tension to the membrane by pulling it towards the gate. We detect the mechanical resonances interferometrically at 633 nm using a network analyzer. We also measure the out-of-plane magnetization of the membrane using magnetic circular dichroism (MCD) at 633 nm. Unless otherwise specified, all measurements were performed at 4 K in a helium exchange gas environment ($<10^{-5}$ Torr). (See Methods for details on device fabrication and measurement techniques.)

Figure 1d shows the fundamental resonance mode of a bilayer CrI₃ membrane at $V_g = 0$. It has a Lorentzian lineshape (solid line) with a peak frequency f around 25.5 MHz and a width around 10 kHz, corresponding to a quality factor of about 2500. The resonance frequency scales inversely with the drumhead radius R , and is determined by stress on the membrane σ and its 2D mass density ρ . Figure 1e shows gate tuning of the resonance frequency, which is well described by the continuum model (assuming zero bending stiffness) with fully clamped boundary: $f = \frac{\xi}{2\pi R} \sqrt{\frac{\sigma}{\rho}}$ (red solid line). Here $\xi \approx 2.405$ is the first root of the zeroth order Bessel function and the stress is obtained by the second derivative of the total energy (elastic plus electrostatic) of the membrane with respect to its vertical displacement. Near $V_g = 0$, the frequency is set by the built-in stress σ_0 , whereas at higher V_g the gate-induced stress $3Y_{eff}\epsilon(V_g)$, which is determined by the effective 2D Young's modulus Y_{eff} and the gate-induced strain $\epsilon(V_g)$, causes the frequency to increase roughly as V_g^4 . This behavior is fully consistent with other 2D NEMS such as graphene and MoS₂ [Ref. ^{22,23,24}]. By calibrating $\epsilon(V_g)$ from the exciton peak shift of the WSe₂ layer (63 meV per % of biaxial strain ²⁵), we determine the basic parameters of the resonator $\sigma_0 \approx 0.5$ N/m, $Y_{eff} \approx 600$ N/m and $\rho \approx 3 \times 10^{-5}$ kg/m² [Ref. ^{22,23,24}] (see Methods).

We investigate the effect of magnetic field on CrI₃ resonators at $V_g = 0$. The nanomechanical resonance of the bilayer CrI₃ device is measured while the field is swept from 1 T to -1 T back to 1 T along \hat{z} (Fig. 2a). The resonance frequency f is independent of field except an abrupt redshift of $\sim 0.06\%$ when the field magnitude exceeds ~ 0.5 T. The linewidth and amplitude basically do not change throughout the entire field range (Supplementary Fig. S1). We correlate the field dependence of f (Fig. 2b) with the membrane MCD (Fig. 2c). The measured MCD is consistent with the reported results for

bilayer CrI₃ [Ref. ¹⁴]. It shows that the membrane is antiferromagnetic (AF) under small fields (the finite MCD signal is caused by layer asymmetry in the heterostructure) and undergoes a first-order AF-FM spin-flip transition (with hysteresis) around ± 0.5 T. The mechanical resonance frequency is thus correlated with the sample's magnetic state with $f_{AF} > f_{FM}$, where f_{AF} and f_{FM} denote the resonance frequency in the AF and FM state, respectively. In contrast to MCD, f is insensitive to the magnetization direction.

Similar behavior is observed in all CrI₃ resonators that were investigated in this study. Figure 2d - 2f shows the corresponding result for a 6-layer CrI₃ resonator under an out-of-plane field up to 2.3 T. A second 6-layer device is shown in Supplementary Fig. S2. Compared to bilayer CrI₃, there are now two spin-flip transitions around 0.9 T and 1.8 T, which correspond to spin flip in the surface layer and the interior layers, respectively ^{9,18}. The resonance frequency redshifts at each spin-flip transition. The total redshift from f_{AF} (~ 0 T) to f_{FM} (> 1.8 T) is about 0.23%. This is nearly 5 times larger than in bilayer CrI₃.

In contrast, the behavior of the resonators under an in-plane magnetic field is distinct. Figure 3a shows the nanomechanical resonance of the same 6-layer CrI₃ device as in Fig. 2d - 2f while the magnetic field is swept from 8 T to -8 T to 8 T along the in-plane direction. The field dependence of f is shown in Fig. 3b after subtraction of a small linear drift due to initial stress relaxation and/or slow temperature drift. Sharp transition and hysteresis that are characteristic for the first-order spin-flip transition are now absent. Instead, f redshifts smoothly with increasing field magnitude and saturates beyond ~ 6 T. This behavior is correlated with the spin-canting effect observed in 2D CrI₃ [Ref. ^{9,18}]. Because of the large out-of-plane magnetic anisotropy, the spins under an in-plane field are canted continuously from \hat{z} until reaching the saturation field, beyond which they are fully aligned with the in-plane field. The total change in f under the in-plane field ($\sim 0.13\%$) is about half of the value under the out-of-plane field for the 6-layer CrI₃ resonator.

The resonance frequency of the NEMS at $V_g = 0$ is determined by the built-in stress σ_0 . The observed correlation between the resonance frequency and the magnetic state of 2D CrI₃ suggests that magnetostriction is a result of competition between minimizing the elastic energy and the internal magnetic interactions. Other effects such as arisen from the magnetostatic energy cannot explain the experimental observations (see Methods). The elastic energy of the membrane per unit area can be expressed as $U = \frac{3}{2} Y_{eff} \epsilon^2$ [Ref. ^{22,23,24}]. Here the effective 2D Young's modulus Y_{eff} is dominated by that of few-layer graphene because of its much higher mechanical stiffness and is independent of magnetic field (Methods); strain $\epsilon = (a - a_0)/a_0$ is defined as the fractional change of the in-plane lattice constant a that conforms to fixed boundary from its equilibrium value a_0 . If we neglect the strain dependence of the demagnetization energy and leave out the intralayer exchange interactions, which do not play a role in the interlayer metamagnetic

transition, the part of free energy that is strain dependent can be expressed for bilayer CrI₃ to the lowest relevant order as

$$F = J_{\perp}(\widehat{\mathbf{S}}_t \cdot \widehat{\mathbf{S}}_b) + K_{eff} \left(|\widehat{\mathbf{S}}_t \times \hat{\mathbf{z}}|^2 + |\widehat{\mathbf{S}}_b \times \hat{\mathbf{z}}|^2 \right). \quad (1)$$

Here $\widehat{\mathbf{S}}_t$ and $\widehat{\mathbf{S}}_b$ denote the spin unit vector of the top and bottom CrI₃ layers, respectively. The two terms describe, respectively, the interlayer exchange coupling with energy per unit area J_{\perp} (> 0) and anisotropy with effective energy per unit area per layer K_{eff} (> 0). For simplicity we only consider the effect of bond length change on J_{\perp} and K_{eff} . The equilibrium lattice constant of the strained membrane in each magnetic state can be found by minimizing the total free energy ($U + F$) with respect to a_0 or equivalently strain ϵ , from which stress ($\sigma_0 = Y_{eff}\epsilon$) and mechanical resonance frequency can be evaluated²⁶ (see Methods).

For spin-flip transitions, the anisotropy energy is not relevant because spins are along the easy axis. Minimizing ($U + F$) for bilayer CrI₃ yields a change in the strain level ($-\frac{2}{3Y_{eff}}\frac{\partial J_{\perp}}{\partial \epsilon}$) and a fractional change in the resonance frequency ($-\frac{1}{3\sigma_0}\frac{\partial J_{\perp}}{\partial \epsilon}$) for the AF-FM transition. We estimate $\frac{\partial J_{\perp}}{\partial \epsilon}A_u \approx -3$ meV, where A_u (≈ 0.47 nm²) is the unit cell area, from the experimental resonance frequency shift and the measured built-in stress σ_0 . The negative sign indicates that strain weakens AF ordering. We also estimate the saturation magnetostriction $|\frac{2}{3Y_{eff}}\frac{\partial J_{\perp}}{\partial \epsilon}| \sim 10^{-6}$ for the bilayer CrI₃ heterostructure. We note that bilayer CrI₃ by itself is expected to have a much higher saturation magnetostriction because of its much smaller Young's modulus compared to graphene.

In 6-layer CrI₃ there are 5 interfaces. The nearly 5-time stronger magnetostrictive response observed in experiment can be understood in terms of a 5-time stronger total interlayer exchange energy $5J_{\perp}(\widehat{\mathbf{S}}_t \cdot \widehat{\mathbf{S}}_b)$ and similar elastic energy compared to the bilayer CrI₃ device. Under an in-plane field, both interlayer exchange and anisotropy contributions to the free energy need to be considered and a similar energy minimization scheme can be applied to yield $-\frac{1}{3\sigma_0}\left(5\frac{\partial J_{\perp}}{\partial \epsilon} + 6\frac{\partial K_{eff}}{\partial \epsilon}\right)$ for the fractional resonance frequency shift. The observed $\sim 50\%$ smaller frequency shift in Fig. 3b compared to Fig. 2e suggests that $\frac{\partial K_{eff}}{\partial \epsilon} \approx -\frac{1}{2}\frac{\partial J_{\perp}}{\partial \epsilon}$ in the 6-layer CrI₃ device.

Finally, we use the NEMS platform to demonstrate strain tuning of magnetism through the inverse magnetostrictive effect. We probe the spin-flip transition in the same bilayer CrI₃ device as in Fig. 2a-c at different V_g 's by MCD. The application of V_g can potentially induce both tension by an electrostatic force and electrostatic doping to the suspended membrane. Figure 4a and 4b compare the behavior of a suspended and substrate-supported region of the membrane. Only the MCD data near the spin-flip transition for

the positive sweeping direction of the field is shown for clarity. For the substrate-supported region, only the electrostatic doping effect is relevant. The spin-flip transition field H_C varies linearly with V_g (red symbols, Fig. 4c), which is in good agreement with previous studies^{14,15}. In contrast, the behavior of the suspended region is symmetric about $V_g = 0$; H_C decreases nonlinearly with magnitude of V_g (blue symbols, Fig. 4c). We conclude from the comparison that electrostatic doping into suspended CrI₃ is negligible and the change in H_C is caused primarily by strain.

Figure 4d shows H_C as a function of gate-induced strain calibrated from the exciton peak shift in the WSe₂ layer. It decreases linearly with strain by as much as ~ 32 mT. Quantitatively, H_C can be related to the interlayer exchange coupling J_{\perp} through $\mu_0 H_C = \frac{J_{\perp} + \mu_0 M_0^2/d}{M_0}$ [Ref. 14], where μ_0 , M_0 and d denote the vacuum permeability, the saturation magnetization per CrI₃ monolayer, and the interlayer distance in bilayer CrI₃, respectively (see Methods). We obtain $\frac{\partial J_{\perp}}{\partial \epsilon} A_u \approx -5$ meV from the slope in Fig. 4d and M_0 by assuming that each Cr³⁺ cation carries a magnetic moment of $3\mu_B$ (Bohr magneton). The value agrees well with that estimated from the mechanical resonance measurement. The discrepancy is largely due to uncertainty in the resonator parameters (such as initial stress and mass). Nevertheless, the good agreement between two independent measurements illustrates the importance of interlayer exchange magnetostriction in 2D CrI₃.

In conclusion, we have demonstrated a new type of magnetostrictive NEMS based on 2D CrI₃. An inverse magnetostrictive effect has also been demonstrated, which allows continuous strain tuning of the internal magnetic interactions. Our results have put in place the groundwork for potential applications of these devices, including magnetic actuation and sensing, as well as a general detection scheme based on mechanical resonances for emerging magnetic states and phase transitions in 2D layered magnetic materials.

Methods

Device fabrication

We used the layer-by-layer dry transfer method to fabricate drumhead resonators made of atomically thin CrI₃ fully encapsulated by few-layer graphene and single-layer WSe₂ as shown in Fig. 1b. Atomically thin flakes of CrI₃, graphene and WSe₂ were mechanically exfoliated onto silicon substrates with a 285-nm oxide layer from the corresponding bulk synthetic crystals (from HQ Graphene). A polymer stamp made of a thin layer of polycarbonate (PC) on polydimethylsiloxane (PDMS) was used to pick up the desired flakes one by one to form the heterostructure. The complete heterostructure was first released onto a new PDMS substrate so that the residual PC film on the sample can be removed by dissolving it in N-Methyl-2-pyrrolidone. The sample was then transferred onto a circular microtrench of $2 - 3 \mu\text{m}$ in radius and 600 nm in depth on a silicon substrate with prepatterned Ti/Au electrodes. A small amount of PDMS residual was left

untreated. CrI_3 was handled inside a nitrogen-filled glovebox with oxygen and water less than 1 part per million (ppm) to avoid degradation. The thickness of atomically thin materials was first estimated by their optical reflection contrast and then measured by atomic force microscopy (AFM). The thickness of CrI_3 flakes was further verified by the magnetization versus out-of-plane magnetic field measurement. The thickness of WSe_2 flakes was verified by optical reflection spectroscopy.

Mechanical resonance detection

An optical interferometric technique was applied to detect the out-of-plane displacement of the resonators^{22,24,27} (Fig. 1a). The resonators were mounted in a closed-cycle cryostat (Attocube, attoDry1000). The output of a HeNe laser at 632.8 nm was focused onto the center of the suspended membrane using a high numerical aperture (N.A. = 0.8) objective. The beam size on the device was on the order of 1 μm and the total power was kept below 1 μW to minimize the laser heating effect. The reflected beam was collected by the same objective and detected by a fast photodetector. Motion of the membrane was actuated capacitively by applying a small r.f. gate voltage (~ 1 mV) between the membrane and the back gate. As the membrane moves in the out-of-plane direction, the optical cavity formed between the membrane and the trenched substrate modulates the device reflectance. The amplitude of the motion as a function of driving frequency was measured by a network analyzer (Agilent E5061A), which both provided the r.f. voltage and measured the fast photodetector response. The amplitude of the motion reaches its maximum when the r.f. frequency matches the natural frequency of the resonator.

Magnetic circular dichroism (MCD) measurements

MCD was employed to characterize the membranes' magnetic properties. A nearly identical optical setup as the one used for the mechanical resonance detection was employed. The polarization of the optical excitation at 632.8 nm was modulated between left and right circular polarization by a photoelastic modulator at 50.1 kHz. Both the a.c. and d.c. component of the reflected beam were detected by a photodiode in combination with a lock-in amplifier and multimeter, respectively. MCD was determined as the ratio of the a.c. and d.c. component.

Strain calibration

Gate-induced strain in the suspended membranes was determined by using monolayer WSe_2 as a strain gauge assuming no relative sliding between the constituent 2D layers. It relies on the fact that the fundamental exciton resonance energy in monolayer WSe_2 redshifts linearly with strain (63 meV/%) for a relatively large range of biaxial strain²⁵. The fundamental exciton energy in monolayer WSe_2 was determined as a function of V_g by optical reflection spectroscopy. In these measurements, broadband radiation from a single-mode fiber-coupled halogen lamp was employed. The collected radiation was detected by a spectrometer equipped with a charge-coupled-device (CCD) camera. The excitation power on the device was kept well below 0.1 μW to minimize the laser heating effect. The exciton resonance energy and the calibrated gate-induced strain as a function of V_g is shown in Supplementary Fig. S3.

Characterization of resonator parameters

By minimizing the sum of the elastic energy and the electrostatic energy with respect to strain (i.e. $\frac{\partial}{\partial \epsilon} \left[\frac{3}{2} Y_{eff} \epsilon^2 - \frac{1}{2} C_g V_g^2 \right] = 0$), we obtain the gate-induced strain $\epsilon(V_g) \approx \frac{1}{96} \left(\frac{R}{D} \right)^2 \left(\frac{\epsilon_0 V_g^2}{D \sigma_0} \right)^2 \propto V_g^4$ for $\epsilon(V_g) \ll \epsilon_0$ (ϵ_0 is the built-in strain). Here C_g is the back gate capacitance, which is strain or gate dependent because of the gate-induced vertical displacement of the membrane, D is the vertical separation between the membrane and the back gate at $V_g = 0$, R is the drumhead radius, and ϵ_0 is the vacuum permittivity. The built-in stress σ_0 can be obtained from the slope of ϵ as a function of V_g^4 (Supplementary Fig. S3c). The effective Young's modulus Y_{eff} and the 2D mass density ρ of the membrane can be obtained by fitting the experimental gate dependence of the resonance frequency $f = \frac{\xi}{2\pi R} \sqrt{\frac{\sigma}{\rho}}$ with $\sigma = \frac{R^2}{4} \frac{\partial^2}{\partial z^2} \left[\frac{3}{2} Y_{eff} \epsilon^2 - \frac{1}{2} C_g V_g^2 \right]$, where z is the vertical displacement [Ref. ^{28,29,30}]. The extracted values for bilayer CrI₃ resonator 1 are $\sigma_0 \approx 0.5 \text{ Nm}^{-1}$, $\rho \approx 3 \times 10^{-5} \text{ kgm}^{-2}$, and $Y_{eff} \approx 600 \text{ Nm}^{-1}$. The mass density is 1.9 times of the expected mass density of the heterostructure presumably due to the presence of polymer residues and other adsorbates on the membrane. The effective Young's modulus is also consistent with the reported values. We estimate the effective Young's modulus of 2D heterostructures as the total contribution of constitute layers, $Y_{eff} = \sum_i n_i Y_{2D,i}$, where n_i and $Y_{2D,i}$ are the layer number and the 2D elastic stiffness of the i -th material per layer. We obtain $Y_{eff} \approx 1200 \text{ Nm}^{-1}$ for bilayer device 1 using $Y_{2D,g} = 340 \text{ Nm}^{-1}$, $Y_{2D,CrI_3} = 25 \text{ Nm}^{-1}$ and $Y_{2D,WSe_2} = 112 \text{ Nm}^{-1}$ reported for the constitute 2D materials [Ref. ^{31,32,33,34}]. The discrepancy may come from the presence of polymer residues and/or wrinkles on the membrane. Most devices studied in this work consist of 3 layers of graphene, 1 layer WSe₂, and 2-6 layers of CrI₃. Y_{eff} is therefore dominated by the contribution of graphene.

Mechanisms for mechanical resonance shift in 2D CrI₃ under a magnetic field

In the main text, we have assigned the competition between the internal magnetic interactions and elastic energy as the major mechanism for the observed mechanical resonance shift in 2D CrI₃ resonators under a magnetic field at $V_g = 0$. Other effects could potentially also give rise to a mechanical resonance shift in 2D CrI₃ under a magnetic field. One such possibility is the magnetostatic pressure from the gradient of the magnetostatic energy in the \hat{z} direction, $\mathbf{M} \cdot \frac{\partial \mathbf{B}}{\partial z}$. Here \mathbf{M} is the sample magnetization and \mathbf{B} is the magnetic field at the sample. However, for a nanometer thick sample with a lateral size of a few microns the gradient is expected to be negligible. This is supported by the absence of field dependence for the mechanical resonance up to high field except at the spin-flip transitions (Supplementary Fig. S4).

Model for exchange magnetostriction in bilayer CrI₃

We consider bilayer CrI₃ under an out-of-plane magnetic field $\mu_0 H$. The free energy per unit area for a free membrane in the AF and FM state in the zero-temperature limit can be expressed as

$$F_{AF} = 2F_0 - J_{\perp}, \quad (\text{S1})$$

$$F_{FM} = 2F_0 + J_{\perp} - 2\mu_0 M_0 \left(H - \frac{M_0}{t} \right). \quad (\text{S2})$$

Here F_0 , M_0 , J_{\perp} and t denote the free energy of each monolayer, saturation magnetization of each monolayer, interlayer exchange interaction, and interlayer distance, respectively. The spin-flip field $\mu_0 H_C$ can be evaluated by requiring $F_{AF} = F_{FM}$ [Ref. ¹³]. The equilibrium lattice constant in the two interlayer magnetic states differs slightly in free membranes. In the presence of fixed boundary, strain is developed with an elastic energy of $U = \frac{3}{2} Y_{eff} \epsilon^2$, where $\epsilon = (a - a_0)/a_0$ is the fractional change of the in-plane lattice constant a (which is fixed by the boundary) from its equilibrium value a_0 . A new equilibrium configuration with lattice constants a_{AF} and a_{FM} is reached for the two magnetic states to minimize the corresponding total free energy ($U + F$) with respect to a_0 . Strain in the AF and FM states ϵ_{AF} and ϵ_{FM} can thus be found by solving the following equations:

$$a_0 \frac{\partial(U+F_{AF})}{\partial a_0} = 2 \frac{\partial F_0}{\partial \epsilon} - \frac{\partial J_{\perp}}{\partial \epsilon} - 3Y_{eff} \epsilon_{AF} = 0. \quad (\text{S3})$$

$$a_0 \frac{\partial(U+F_{FM})}{\partial a_0} = 2 \frac{\partial F_0}{\partial \epsilon} + \frac{\partial J_{\perp}}{\partial \epsilon} - 3Y_{eff} \epsilon_{FM} = 0. \quad (\text{S4})$$

The derivatives are evaluated at the equilibrium lattice constants. Note that $a_0 \frac{\partial U}{\partial a_0} = -\frac{\partial U}{\partial \epsilon}$ for the fixed boundary condition (i.e. a is a constant), and the strain dependence of M_0 is ignored. Therefore, the strain difference between the two states is

$$\epsilon_{AF} - \epsilon_{FM} = -\frac{2}{3Y_{eff}} \frac{\partial J_{\perp}}{\partial \epsilon}. \quad (\text{S5})$$

And the fractional change in the resonance frequency is given by

$$\frac{f_{AF} - f_{FM}}{f_{AF}} \approx \frac{\sigma_{AF} - \sigma_{FM}}{2\sigma_{AF}} = -\frac{1}{3\sigma_0} \frac{\partial J_{\perp}}{\partial \epsilon}, \quad (\text{S6})$$

since $f \propto \sqrt{\sigma}$. Here we have taken the initial state to be AF. The effect of magnetic anisotropy under in-plane magnetic field can be taken into account in a similar manner.

References

-
- ¹ Craighead, H. G. Nanoelectromechanical Systems. *Science* **290**, 1532–1535 (2000).
 - ² Ekinici, K. L. & Roukes, M. L. Nanoelectromechanical systems. *Rev. Sci. Instrum.* **76**, 061101 (2005).
 - ³ Mak, K. F., Shan, J. & Ralph, D. C. Probing and controlling magnetic states in 2D layered magnetic materials. *Nat. Rev. Phys.* **1**, 646–661 (2019).

-
- ⁴ Gong, C. et al. Discovery of intrinsic ferromagnetism in two-dimensional van der Waals crystals. *Nature* **546**, 265–269 (2017).
- ⁵ Huang, B. et al. Layer-dependent ferromagnetism in a van der Waals crystal down to the monolayer limit. *Nature* **546**, 270–273 (2017).
- ⁶ Gong, C. & Zhang, X. Two-dimensional magnetic crystals and emergent heterostructure devices. *Science*. **363**, eaav4450 (2019).
- ⁷ Gibertini, M., Koperski, M., Morpurgo, A. F. & Novoselov, K. S. Magnetic 2D materials and heterostructures. *Nat. Nanotechnol.* **14**, 408–419 (2019).
- ⁸ Burch, K. S., Mandrus, D. & Park, J.-G. Magnetism in two-dimensional van der Waals materials. *Nature* **563**, 47–52 (2018).
- ⁹ Song, T. et al., Giant tunneling magnetoresistance in spin-filter van der Waals heterostructures. *Science* **360**, 1214–1218 (2018)
- ¹⁰ Klein, D. R. et al., Probing magnetism in 2D van der Waals crystalline insulators via electron tunneling. *Science* **360**, 1218–1222 (2018)
- ¹¹ Kim, H. H. et al., One million percent tunnel magnetoresistance in a magnetic van der Waals heterostructure. *Nano Lett.* **18**, 4885–4890 (2018)
- ¹² Wang, Z. et al., Very large tunneling magnetoresistance in layered magnetic semiconductor CrI₃. *Nat. Commun.* **9**, 2516 (2018)
- ¹³ Jiang, S., Shan, J., Mak, K. F., Electric-field switching of two-dimensional van der Waals magnets. *Nat. Mater.* **17**, 406–410 (2018)
- ¹⁴ Jiang, S., Li, L., Wang, Z., Mak, K. F. & Shan, J. Controlling magnetism in 2D CrI₃ by electrostatic doping. *Nat. Nanotechnol.* **13**, 549–553 (2018).
- ¹⁵ Huang, B. et al. Electrical control of 2D magnetism in bilayer CrI₃. *Nat. Nanotechnol.* **13**, 544–548 (2018)
- ¹⁶ Jin, C. et al. Imaging and control of critical spin fluctuations in two-dimensional magnets, [arXiv:1910.13023](https://arxiv.org/abs/1910.13023).
- ¹⁷ Wang, Z. *et al.* Electric-field control of magnetism in a few-layered van der Waals ferromagnetic semiconductor. *Nat. Nanotechnol.* **13**, 554–559 (2018).
- ¹⁸ Jiang, S., Li, L., Wang, Z., Mak, K. F. & Shan, J. Spin transistor built on 2D van der Waals heterostructures. *Nat. Electron.* **2**, 159–163 (2019).
- ¹⁹ Šiškins, M. et al, Magnetic and electronic phase transitions probed by nanomechanical resonance, [arXiv:1911.08537](https://arxiv.org/abs/1911.08537)
- ²⁰ Myung, N. V., Park, D.-Y., Yoo, B.-Y. & Sumodjo, P. T. A. Development of electroplated magnetic materials for MEMS. *J. Magn. Magn. Mater.* **265**, 189–198 (2003).
- ²¹ Zorman, C. A. & Mehregany, M. Materials Aspects of Micro- and Nanoelectromechanical Systems. in Springer Handbook of Nanotechnology 203–224 (Springer Berlin Heidelberg, 2004).
- ²² Bunch, J. S. *et al.* Electromechanical Resonators from Graphene Sheets. *Science* **315**, 490–493 (2007).
- ²³ Chen, C. *et al.* Performance of monolayer graphene nanomechanical resonators with electrical readout. *Nat. Nanotechnol.* **4**, 861–867 (2009).
- ²⁴ Lee, J. *et al.* Electrically tunable single- and few-layer MoS₂ nanoelectromechanical systems with broad dynamic range. *Sci. Adv.* **4**, eaao6653 (2018).

-
- ²⁵ Frisenda, R. *et al.* Biaxial strain tuning of the optical properties of single-layer transition metal dichalcogenides. *npj 2D Mater. Appl.* **1**, 10 (2017).
- ²⁶ Kittel, C. Model of Exchange-Inversion Magnetization. *Phys. Rev.* **120**, 335–342 (1960).
- ²⁷ Storch, I. R. *et al.* Young's modulus and thermal expansion of tensioned graphene membranes. *Phys. Rev. B* **98**, 085408 (2018).
- ²⁸ Bunch, J. S. *et al.* Electromechanical Resonators from Graphene Sheets. *Science* **315**, 490–493 (2007).
- ²⁹ Chen, C. *et al.* Performance of monolayer graphene nanomechanical resonators with electrical readout. *Nat. Nanotechnol.* **4**, 861–867 (2009).
- ³⁰ Lee, J. *et al.* Electrically tunable single- and few-layer MoS₂ nanoelectromechanical systems with broad dynamic range. *Sci. Adv.* **4**, eaao6653 (2018).
- ³¹ Lee, C., Wei, X., Kysar, J. W. & Hone, J. Measurement of the Elastic Properties and Intrinsic Strength of Monolayer Graphene. *Science* **321**, 385–388 (2008).
- ³² Liu, J., Sun, Q., Kawazoe, Y. & Jena, P. Exfoliating biocompatible ferromagnetic Cr-trihalide monolayers. *Phys. Chem. Chem. Phys.* **18**, 8777–8784 (2016).
- ³³ Zheng, F. *et al.* Tunable spin states in the two-dimensional magnet CrI₃. *Nanoscale* **10**, 14298–14303 (2018).
- ³⁴ Zhang, R., Koutsos, V. & Cheung, R. Elastic properties of suspended multilayer WSe₂. *Appl. Phys. Lett.* **108**, 042104 (2016).

Competing interests

The authors declare no competing interests.

Data availability

The data that support the findings of this study are available within the paper and its Supplementary Information. Additional data are available from the corresponding authors upon request.

Figures and figure captions

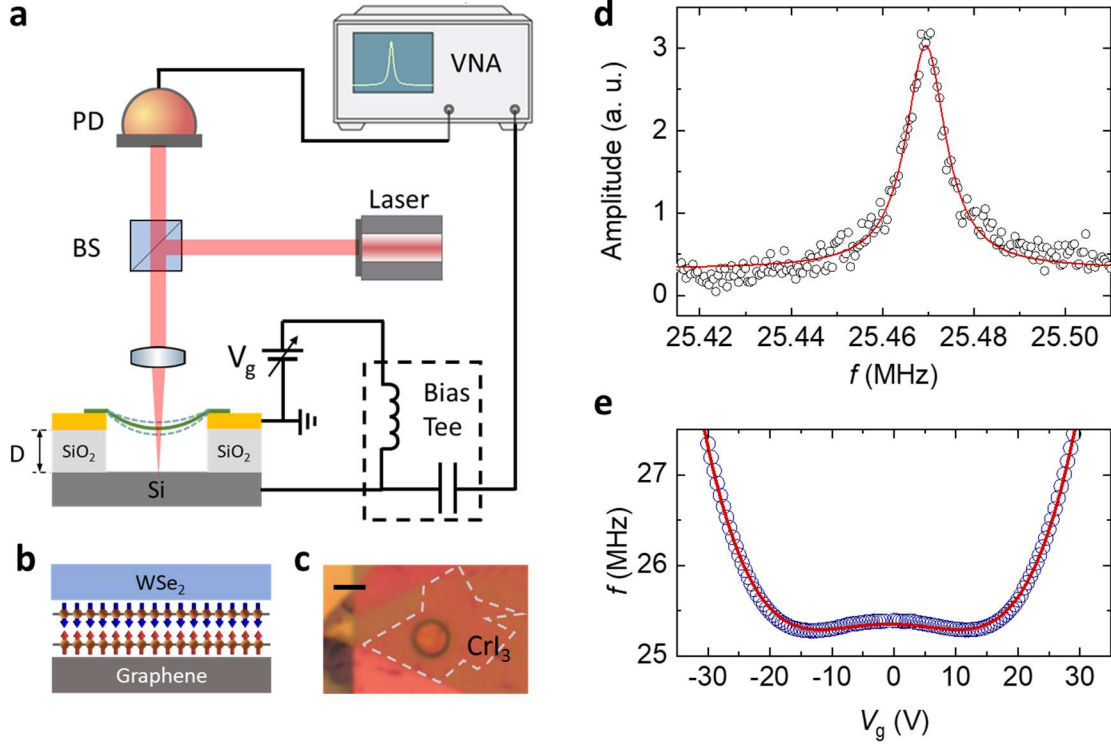


Fig. 1: 2D CrI₃ nanoelectromechanical resonators. **a**, Schematic of the measurement system. The resonator (suspended 2D membrane on a Si trench of depth D) is actuated by an r.f. voltage from a vector network analyzer (VNA) through a bias tee. A DC voltage V_g is superimposed to apply static tension to the membrane. The motion is detected interferometrically by a HeNe laser, which is focused onto the center of the resonator. BS: beam splitter; PD: photodetector. **b**, Schematic of a bilayer CrI₃ resonator with AF CrI₃ encapsulated by few-layer graphene and monolayer WSe₂. Filled spheres and arrows denote Cr atoms and spins in the top and bottom CrI₃ layer. **c**, Optical microscope image of a bilayer CrI₃ device suspended over a circular trench. Dashed line shows the boundary of the CrI₃ flake. Scale bar is 4 μm . **d**, Fundamental mechanical resonance (symbols) of bilayer CrI₃ resonator 1 (radius 2 μm) and a Lorentzian fit of the resonance spectrum (solid line). **e**, Gate dependence of the measured resonance frequency (symbols) and fit to the continuum model (solid line) with $\sigma_0 \approx 0.5 \text{ Nm}^{-1}$, $\rho \approx 3 \times 10^{-5} \text{ kgm}^{-2}$ (1.9 times the mass density of the membrane) and $Y_{eff} \approx 600 \text{ Nm}^{-1}$.

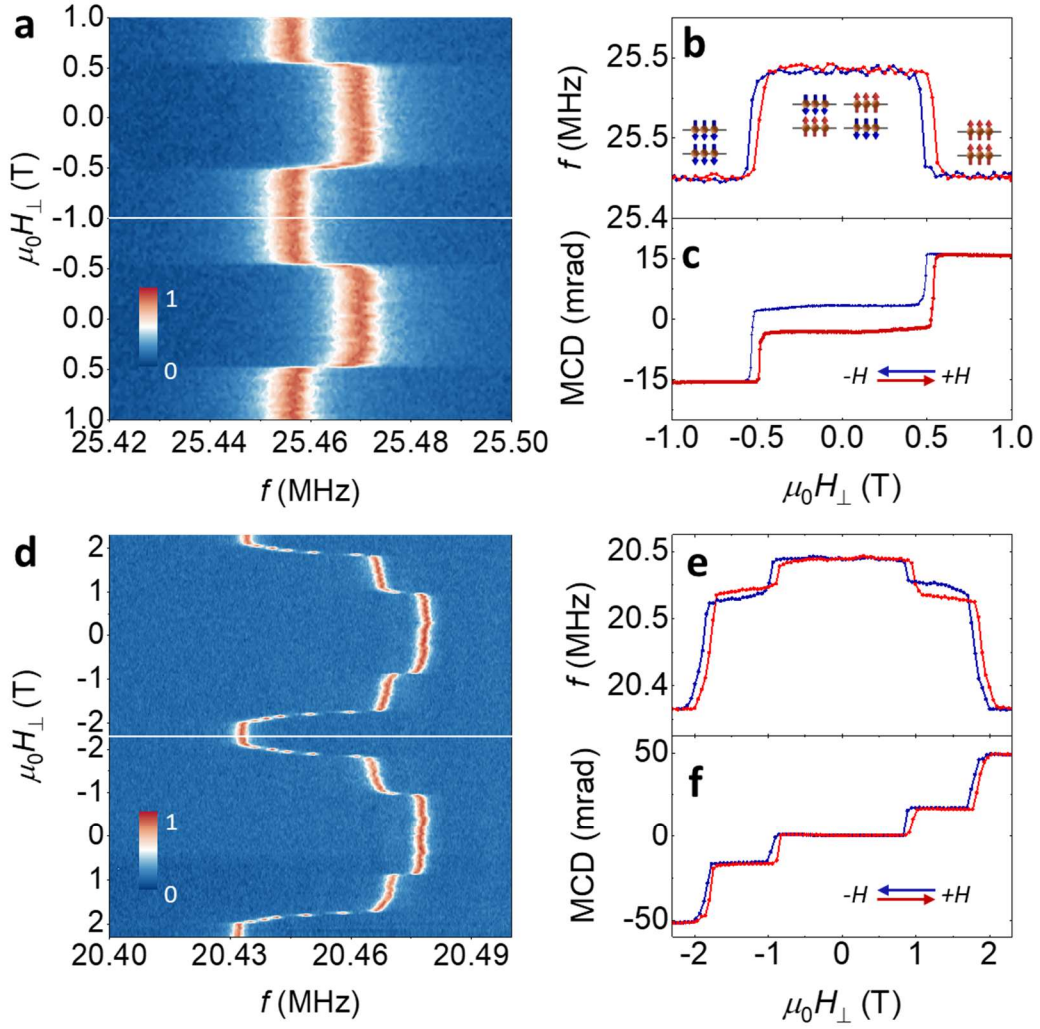


Fig. 2: Mechanical detection of the spin-flip transition in 2D CrI₃. **a**, Normalized vibration amplitude of bilayer CrI₃ resonator 1 vs. driving frequency under an out of-plane magnetic field ($\mu_0 H_{\perp}$) that sweeps from 1 T to -1 T to 1 T. **b**, Resonance frequency f extracted from **a** as a function of magnetic field. **c**, MCD of the membrane as a function of magnetic field. The red and blue lines in **b** and **c** correspond to the measurement for the positive and negative sweeping directions of the field, respectively. **d-f**, Same measurements as in **a-c** for 6-layer CrI₃ resonator 1 (radius 3 μm).

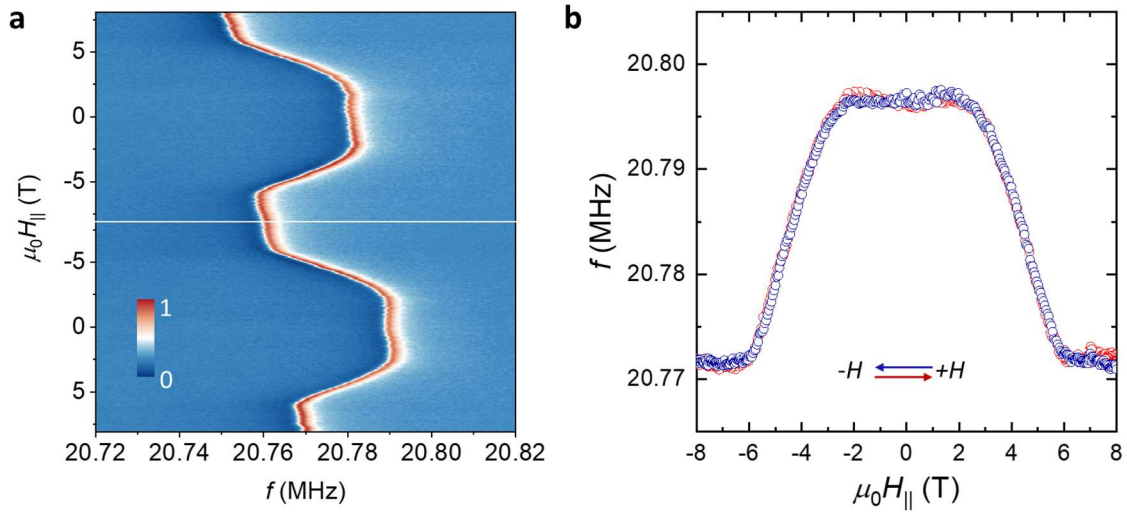


Fig. 3: Mechanical detection of spin canting in 2D CrI₃. **a**, Normalized vibration amplitude vs. driving frequency under an in-plane magnetic field ($\mu_0 H_{\parallel}$) that sweeps from 8 T to -8 T to 8 T for 6-layer CrI₃ resonator 1. **b**, Resonance frequency f extracted from **a** as a function of magnetic field. Red and blue lines correspond to the measurement for the positive and negative sweeping directions of the field, respectively.

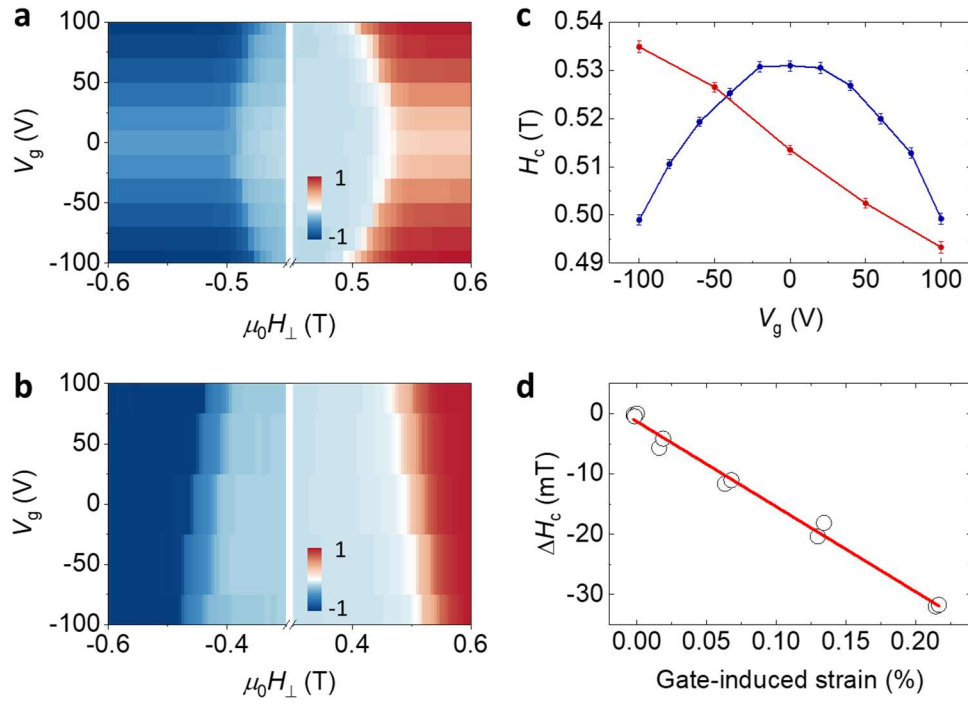
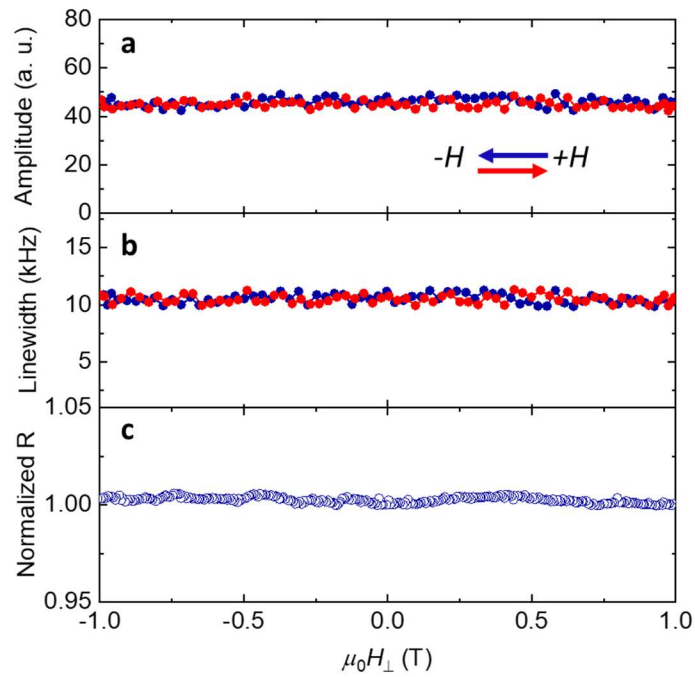
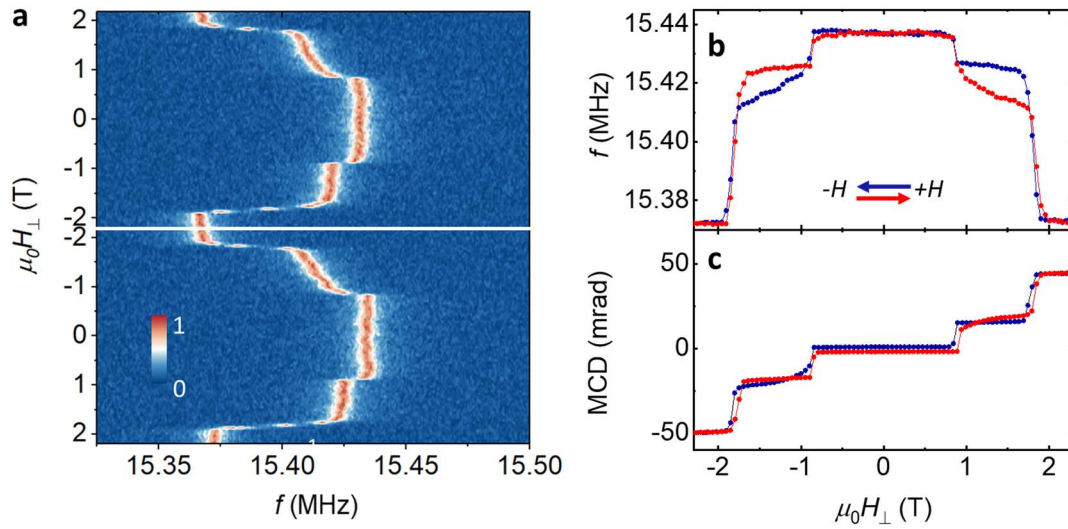


Fig. 4: Strain tuning of the spin-flip transition in 2D CrI₃. **a, b**, Normalized MCD as a function of out-of-plane magnetic field ($\mu_0 H_{\perp}$) that sweeps from - 1 T to 1 T (only - 0.6 T to 0.6 T is shown here for clarity) at different V_g 's for a suspended (**a**) and substrate-supported region (**b**) of bilayer CrI₃ resonator 1. **c**, Spin-flip transition field as a function of gate voltage for the suspended (blue) and substrate-supported (red) region of the membrane. The lines are a guide to the eye. **d**, Spin-flip transition field as a function of gate-induced strain (symbols). The solid line is a linear fit.

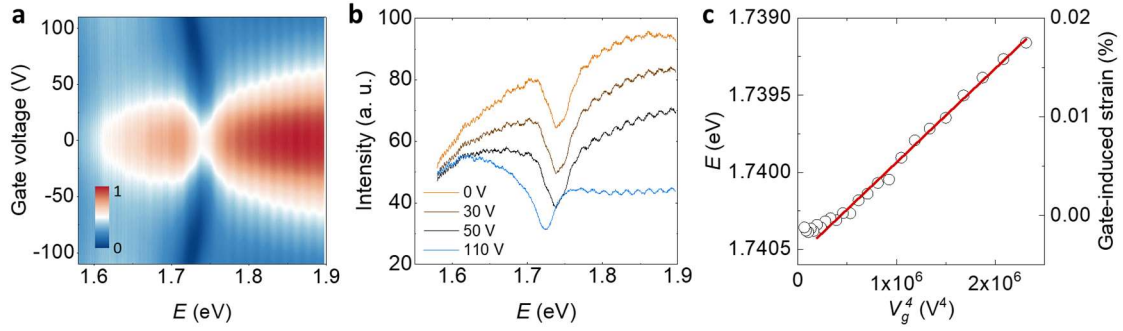
Supplementary figures and figure captions



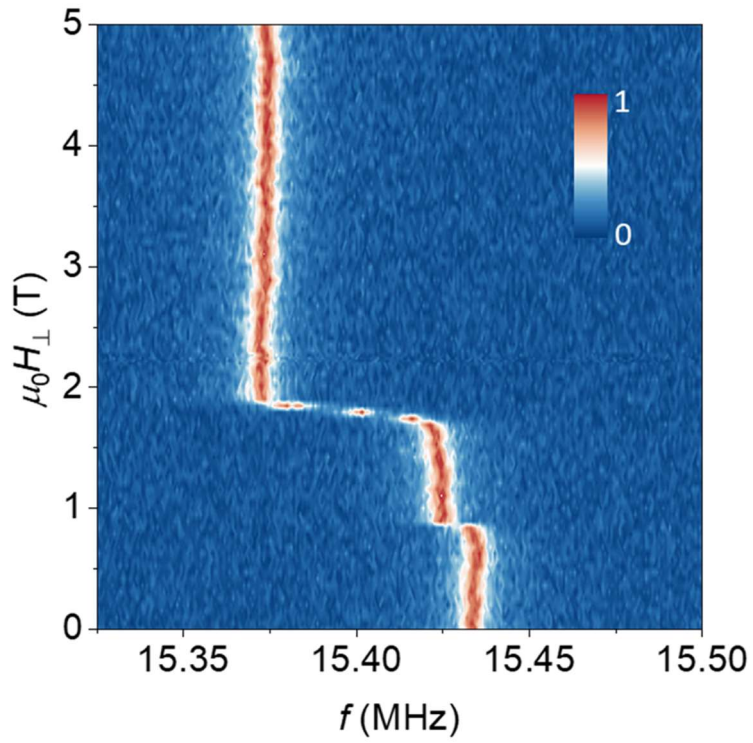
Supplementary Fig. S1: Mechanical resonance of 2D CrI₃ under an out-of-plane magnetic field. **a, b,** Field dependence of the amplitude (**a**) and linewidth (**b**) of the fundamental resonance of bilayer CrI₃ resonator 1. The field dependence of the resonance frequency is shown in Fig. 2b. The red and blue symbols correspond to the measurement for the positive and negative sweeping directions of the field, respectively. **c,** Field dependence of the reflectance at 633 nm normalized by the reflectance at zero field.



Supplementary Fig. S2: Results for 6-layer CrI₃ resonator 2 under an out-of-plane magnetic field. **a**, Normalized vibration amplitude vs. driving frequency under an out of-plane magnetic field ($\mu_0 H_{\perp}$) that sweeps from 2.3 T to -2.3 T to 2.3 T at $V_g = 0$ V. **b**, Resonance frequency f extracted from **a** as a function of magnetic field. **c**, MCD of the membrane as a function of magnetic field at $V_g = 0$ V. The red and blue lines in **b**, **c** correspond to the measurement for the positive and negative sweeping directions of the field, respectively. The radius of the drumhead is 3 μm .



Supplementary Fig. S3: Strain calibration and determination of resonator parameters. **a**, Reflection contrast of bilayer CrI₃ resonator 1 from 1.6 – 1.9 eV as a function of gate voltage. The main feature is a dip (around 1.75 eV at $V_g = 0$ V), which corresponds to the fundamental exciton resonance of monolayer WSe₂. The feature redshifts slightly with V_g up to about 40 V followed by a much larger redshift with further increase of V_g . **b**, Representative spectra at selected V_g . **c**, Exciton resonance energy extracted from **a** (left axis) and gate-induced strain calibrated from the exciton resonance energy (right axis) as a function of V_g^4 for V_g up to 39 V. The solid line is a linear fit from the slope of which the built-in stress σ_0 was determined.



Supplementary Fig. S4: 2D CrI₃ resonators under high out-of-plane fields. Normalized vibration amplitude vs. driving frequency under an out of-plane magnetic field up to 5 T for 6-layer CrI₃ resonator 1. The resonance frequency, amplitude and linewidth basically do not change up to 5 T except at the spin-flip transitions.